

Study of Jet Shapes
in Inclusive Jet Production in $p\bar{p}$ Collisions at $\sqrt{s} = 1.96$ TeV

D. Acosta,¹⁶ J. Adelman,¹² T. Affolder,⁹ T. Akimoto,⁵⁴ M.G. Albrow,¹⁵ D. Ambrose,¹⁵ S. Amerio,⁴² D. Amidei,³³
A. Anastassov,⁵⁰ K. Anikeev,¹⁵ A. Annovi,⁴⁴ J. Antos,¹ M. Aoki,⁵⁴ G. Apollinari,¹⁵ T. Arisawa,⁵⁶ J-F. Arguin,³²
A. Artikov,¹³ W. Ashmanskas,¹⁵ A. Attal,⁷ F. Azfar,⁴¹ P. Azzi-Bacchetta,⁴² N. Bacchetta,⁴² H. Bachacou,²⁸
W. Badgett,¹⁵ A. Barbaro-Galtieri,²⁸ G.J. Barker,²⁵ V.E. Barnes,⁴⁶ B.A. Barnett,²⁴ S. Baroiant,⁶ G. Bauer,³¹
F. Bedeschi,⁴⁴ S. Behari,²⁴ S. Belforte,⁵³ G. Bellettini,⁴⁴ J. Bellinger,⁵⁸ A. Belloni,³¹ E. Ben-Haim,¹⁵ D. Benjamin,¹⁴
A. Beretvas,¹⁵ T. Berry,²⁹ A. Bhatti,⁴⁸ M. Binkley,¹⁵ D. Bisello,⁴² M. Bishai,¹⁵ R.E. Blair,² C. Blocker,⁵ K. Bloom,³³
B. Blumenfeld,²⁴ A. Bocci,⁴⁸ A. Bodek,⁴⁷ G. Bolla,⁴⁶ A. Bolshov,³¹ D. Bortoletto,⁴⁶ J. Boudreau,⁴⁵ S. Bourov,¹⁵
B. Brau,⁹ C. Bromberg,³⁴ E. Brubaker,¹² J. Budagov,¹³ H.S. Budd,⁴⁷ K. Burkett,¹⁵ G. Busetto,⁴² P. Bussey,¹⁹
K.L. Byrum,² S. Cabrera,¹⁴ M. Campanelli,¹⁸ M. Campbell,³³ F. Canelli,⁷ A. Canepa,⁴⁶ M. Casarsa,⁵³ D. Carlsmith,⁵⁸
R. Carosi,⁴⁴ S. Carron,¹⁴ M. Cavalli-Sforza,³ A. Castro,⁴ P. Catastini,⁴⁴ D. Cauz,⁵³ A. Cerri,²⁸ L. Cerrito,⁴¹
J. Chapman,³³ Y.C. Chen,¹ M. Chertok,⁶ G. Chiarelli,⁴⁴ G. Chlachidze,¹³ F. Chlebana,¹⁵ I. Cho,²⁷ K. Cho,²⁷
D. Chokheli,¹³ J.P. Chou,²⁰ S. Chuang,⁵⁸ K. Chung,¹¹ W-H. Chung,⁵⁸ Y.S. Chung,⁴⁷ M. Cijliak,⁴⁴ C.I. Ciobanu,²³
M.A. Ciocci,⁴⁴ A.G. Clark,¹⁸ D. Clark,⁵ M. Coca,¹⁴ A. Connolly,²⁸ M. Convery,⁴⁸ J. Conway,⁶ B. Cooper,³⁰ K. Copic,³³
M. Cordelli,¹⁷ G. Cortiana,⁴² J. Cranshaw,⁵² J. Cuevas,¹⁰ A. Cruz,¹⁶ R. Culbertson,¹⁵ C. Currat,²⁸ D. Cyr,⁵⁸
D. Dagenhart,⁵ S. Da Ronco,⁴² S. D'Auria,¹⁹ P. de Barbaro,⁴⁷ S. De Cecco,⁴⁹ A. Deisher,²⁸ G. De Lentdecker,⁴⁷
M. Dell'Orso,⁴⁴ S. Demers,⁴⁷ L. Demortier,⁴⁸ M. Deninno,⁴ D. De Pedis,⁴⁹ P.F. Derwent,¹⁵ C. Dionisi,⁴⁹
J.R. Dittmann,¹⁵ P. DiTuro,⁵⁰ C. Dörr,²⁵ A. Dominguez,²⁸ S. Donati,⁴⁴ M. Donega,¹⁸ J. Donini,⁴² M. D'Onofrio,¹⁸
T. Dorigo,⁴² K. Ebina,⁵⁶ J. Efron,³⁸ J. Ehlers,¹⁸ R. Erbacher,⁶ M. Erdmann,²⁵ D. Errede,²³ S. Errede,²³ R. Eusebi,⁴⁷
H-C. Fang,²⁸ S. Farrington,²⁹ I. Fedorko,⁴⁴ W.T. Fedorko,¹² R.G. Feild,⁵⁹ M. Feindt,²⁵ J.P. Fernandez,⁴⁶ R.D. Field,¹⁶
G. Flanagan,³⁴ L.R. Flores-Castillo,⁴⁵ A. Foland,²⁰ S. Forrester,⁶ G.W. Foster,¹⁵ M. Franklin,²⁰ J.C. Freeman,²⁸
Y. Fujii,²⁶ I. Furic,¹² A. Gajjar,²⁹ M. Gallinaro,⁴⁸ J. Galyardt,¹¹ M. Garcia-Sciveres,²⁸ A.F. Garfinkel,⁴⁶ C. Gay,⁵⁹
H. Gerberich,¹⁴ D.W. Gerdes,³³ E. Gerchtein,¹¹ S. Giagu,⁴⁹ P. Giannetti,⁴⁴ A. Gibson,²⁸ K. Gibson,¹¹ C. Ginsburg,¹⁵
K. Giolo,⁴⁶ M. Giordani,⁵³ M. Giunta,⁴⁴ G. Giurgiu,¹¹ V. Glagolev,¹³ D. Glenzinski,¹⁵ M. Gold,³⁶ N. Goldschmidt,³³
D. Goldstein,⁷ J. Goldstein,⁴¹ G. Gomez,¹⁰ G. Gomez-Ceballos,¹⁰ M. Goncharov,⁵¹ O. González,⁴⁶ I. Gorelov,³⁶
A.T. Goshaw,¹⁴ Y. Gotra,⁴⁵ K. Goulianos,⁴⁸ A. Gresele,⁴² M. Griffiths,²⁹ C. Grosso-Pilcher,¹² U. Grundler,²³
J. Guimaraes da Costa,²⁰ C. Haber,²⁸ K. Hahn,⁴³ S.R. Hahn,¹⁵ E. Halkiadakis,⁴⁷ A. Hamilton,³² B-Y. Han,⁴⁷

R. Handler,⁵⁸ F. Happacher,¹⁷ K. Hara,⁵⁴ M. Hare,⁵⁵ R.F. Harr,⁵⁷ R.M. Harris,¹⁵ F. Hartmann,²⁵ K. Hatakeyama,⁴⁸
 J. Hauser,⁷ C. Hays,¹⁴ H. Hayward,²⁹ B. Heinemann,²⁹ J. Heinrich,⁴³ M. Hennecke,²⁵ M. Herndon,²⁴ C. Hill,⁹
 D. Hirschbuehl,²⁵ A. Hocker,¹⁵ K.D. Hoffman,¹² A. Holloway,²⁰ S. Hou,¹ M.A. Houlden,²⁹ B.T. Huffman,⁴¹
 Y. Huang,¹⁴ R.E. Hughes,³⁸ J. Huston,³⁴ K. Ikado,⁵⁶ J. Incandela,⁹ G. Introzzi,⁴⁴ M. Iori,⁴⁹ Y. Ishizawa,⁵⁴ C. Issever,⁹
 A. Ivanov,⁶ Y. Iwata,²² B. Iyutin,³¹ E. James,¹⁵ D. Jang,⁵⁰ B. Jayatilaka,³³ D. Jeans,⁴⁹ H. Jensen,¹⁵ E.J. Jeon,²⁷
 M. Jones,⁴⁶ K.K. Joo,²⁷ S.Y. Jun,¹¹ T. Junk,²³ T. Kamon,⁵¹ J. Kang,³³ M. Karagoz Unel,³⁷ P.E. Karchin,⁵⁷
 Y. Kato,⁴⁰ Y. Kemp,²⁵ R. Kephart,¹⁵ U. Kerzel,²⁵ V. Khotilovich,⁵¹ B. Kilminster,³⁸ D.H. Kim,²⁷ H.S. Kim,²³
 J.E. Kim,²⁷ M.J. Kim,¹¹ M.S. Kim,²⁷ S.B. Kim,²⁷ S.H. Kim,⁵⁴ Y.K. Kim,¹² M. Kirby,¹⁴ L. Kirsch,⁵ S. Klimenko,¹⁶
 M. Klute,³¹ B. Knuteson,³¹ B.R. Ko,¹⁴ H. Kobayashi,⁵⁴ D.J. Kong,²⁷ K. Kondo,⁵⁶ J. Konigsberg,¹⁶ K. Kordas,³²
 A. Korn,³¹ A. Korytov,¹⁶ A.V. Kotwal,¹⁴ A. Kovalev,⁴³ J. Kraus,²³ I. Kravchenko,³¹ A. Kreymer,¹⁵ J. Kroll,⁴³
 M. Kruse,¹⁴ V. Krutelyov,⁵¹ S.E. Kuhlmann,² S. Kwang,¹² A.T. Laasanen,⁴⁶ S. Lai,³² S. Lami,^{44,48} S. Lammel,¹⁵
 M. Lancaster,³⁰ R. Lander,⁶ K. Lannon,³⁸ A. Lath,⁵⁰ G. Latino,⁴⁴ I. Lazzizzera,⁴² C. Lecci,²⁵ T. LeCompte,²
 J. Lee,²⁷ J. Lee,⁴⁷ S.W. Lee,⁵¹ R. Lefèvre,³ N. Leonardo,³¹ S. Leone,⁴⁴ S. Levy,¹² J.D. Lewis,¹⁵ K. Li,⁵⁹
 C. Lin,⁵⁹ C.S. Lin,¹⁵ M. Lindgren,¹⁵ E. Lipeles,⁸ T.M. Liss,²³ A. Lister,¹⁸ D.O. Litvintsev,¹⁵ T. Liu,¹⁵ Y. Liu,¹⁸
 N.S. Lockyer,⁴³ A. Loginov,³⁵ M. Loreti,⁴² P. Loverre,⁴⁹ R-S. Lu,¹ D. Lucchesi,⁴² P. Lujan,²⁸ P. Lukens,¹⁵ G. Lungu,¹⁶
 L. Lyons,⁴¹ J. Lys,²⁸ R. Lysak,¹ E. Lytken,⁴⁶ D. MacQueen,³² R. Madrak,¹⁵ K. Maeshima,¹⁵ P. Maksimovic,²⁴
 G. Manca,²⁹ F. Margaroli,⁴ R. Marginean,¹⁵ C. Marino,²³ A. Martin,⁵⁹ M. Martin,²⁴ V. Martin,³⁷ M. Martínez,³
 T. Maruyama,⁵⁴ H. Matsunaga,⁵⁴ M. Mattson,⁵⁷ P. Mazzanti,⁴ K.S. McFarland,⁴⁷ D. McGivern,³⁰ P.M. McIntyre,⁵¹
 P. McNamara,⁵⁰ R. McNulty,²⁹ A. Mehta,²⁹ S. Menzemer,³¹ A. Menzione,⁴⁴ P. Merkel,⁴⁶ C. Mesropian,⁴⁸ A. Messina,⁴⁹
 T. Miao,¹⁵ N. Miladinovic,⁵ J. Miles,³¹ L. Miller,²⁰ R. Miller,³⁴ J.S. Miller,³³ C. Mills,⁹ R. Miquel,²⁸ S. Miscetti,¹⁷
 G. Mitselmakher,¹⁶ A. Miyamoto,²⁶ N. Moggi,⁴ B. Mohr,⁷ R. Moore,¹⁵ M. Morello,⁴⁴ P.A. Movilla Fernandez,²⁸
 J. Muelmenstaedt,²⁸ A. Mukherjee,¹⁵ M. Mulhearn,³¹ T. Muller,²⁵ R. Mumford,²⁴ A. Munar,⁴³ P. Murat,¹⁵
 J. Nachtman,¹⁵ S. Nahn,⁵⁹ I. Nakano,³⁹ A. Napier,⁵⁵ R. Napura,²⁴ D. Naumov,³⁶ V. Necula,¹⁶ J. Nielsen,²⁸
 T. Nelson,¹⁵ C. Neu,⁴³ M.S. Neubauer,⁸ T. Nigmanov,⁴⁵ L. Nodulman,² O. Norriella,³ T. Ogawa,⁵⁶ S.H. Oh,¹⁴
 Y.D. Oh,²⁷ T. Ohsugi,²² T. Okusawa,⁴⁰ R. Oldeman,²⁹ R. Orava,²¹ W. Orejudos,²⁸ K. Osterberg,²¹ C. Pagliarone,⁴⁴
 E. Palencia,¹⁰ R. Paoletti,⁴⁴ V. Papadimitriou,¹⁵ A.A. Paramonov,¹² S. Pashapour,³² J. Patrick,¹⁵ G. Pauletta,⁵³
 M. Paulini,¹¹ C. Paus,³¹ D. Pellett,⁶ A. Penzo,⁵³ T.J. Phillips,¹⁴ G. Piacentino,⁴⁴ J. Piedra,¹⁰ K.T. Pitts,²³ C. Plager,⁷
 L. Pondrom,⁵⁸ G. Pope,⁴⁵ X. Portell,³ O. Poukhov,¹³ N. Pounder,⁴¹ F. Prakoshyn,¹³ A. Pronko,¹⁶ J. Proudfoot,²
 F. Ptohos,¹⁷ G. Punzi,⁴⁴ J. Rademacker,⁴¹ M.A. Rahaman,⁴⁵ A. Rakitine,³¹ S. Rappoccio,²⁰ F. Ratnikov,⁵⁰ H. Ray,³³

B. Reiser¹⁵ V. Rekovic,³⁶ P. Renton,⁴¹ M. Rescigno,⁴⁹ F. Rimondi,⁴ K. Rinnert,²⁵ L. Ristori,⁴⁴ W.J. Robertson,¹⁴ A. Robson,¹⁹ T. Rodrigo,¹⁰ S. Rolli,⁵⁵ R. Roser,¹⁵ R. Rossin,¹⁶ C. Rott,⁴⁶ J. Russ,¹¹ V. Rusu,¹² A. Ruiz,¹⁰ D. Ryan,⁵⁵ H. Saarikko,²¹ S. Sabik,³² A. Safonov,⁶ R. St. Denis,¹⁹ W.K. Sakumoto,⁴⁷ G. Salamanna,⁴⁹ D. Saltzberg,⁷ C. Sanchez,³ L. Santi,⁵³ S. Sarkar,⁴⁹ K. Sato,⁵⁴ P. Savard,³² A. Savoy-Navarro,¹⁵ P. Schlabach,¹⁵ E.E. Schmidt,¹⁵ M.P. Schmidt,⁵⁹ M. Schmitt,³⁷ T. Schwarz,³³ L. Scodellaro,¹⁰ A.L. Scott,⁹ A. Scribano,⁴⁴ F. Scuri,⁴⁴ A. Sedov,⁴⁶ S. Seidel,³⁶ Y. Seiya,⁴⁰ A. Semenov,¹³ F. Semeria,⁴ L. Sexton-Kennedy,¹⁵ I. Sfiligoi,¹⁷ M.D. Shapiro,²⁸ T. Shears,²⁹ P.F. Shepard,⁴⁵ D. Sherman,²⁰ M. Shimojima,⁵⁴ M. Shochet,¹² Y. Shon,⁵⁸ I. Shreyber,³⁵ A. Sidoti,⁴⁴ A. Sill,⁵² P. Sinervo,³² A. Sisakyan,¹³ J. Sjolin,⁴¹ A. Skiba,²⁵ A.J. Slaughter,¹⁵ K. Sliwa,⁵⁵ D. Smirnov,³⁶ J.R. Smith,⁶ F.D. Snider,¹⁵ R. Snihur,³² M. Soderberg,³³ A. Soha,⁶ S.V. Somalwar,⁵⁰ J. Spalding,¹⁵ M. Spezziga,⁵² F. Spinella,⁴⁴ P. Squillacioti,⁴⁴ H. Stadie,²⁵ M. Stanitzki,⁵⁹ B. Stelzer,³² O. Stelzer-Chilton,³² D. Stentz,³⁷ J. Strologas,³⁶ D. Stuart,⁹ J. S. Suh,²⁷ A. Sukhanov,¹⁶ K. Sumorok,³¹ H. Sun,⁵⁵ T. Suzuki,⁵⁴ A. Taffard,²³ R. Tafirout,³² H. Takano,⁵⁴ R. Takashima,³⁹ Y. Takeuchi,⁵⁴ K. Takikawa,⁵⁴ M. Tanaka,² R. Tanaka,³⁹ N. Tanimoto,³⁹ M. Tecchio,³³ P.K. Teng,¹ K. Terashi,⁴⁸ R.J. Tesarek,¹⁵ S. Tether,³¹ J. Thom,¹⁵ A.S. Thompson,¹⁹ E. Thomson,⁴³ P. Tipton,⁴⁷ V. Tiwari,¹¹ S. Tkaczyk,¹⁵ D. Toback,⁵¹ K. Tollefson,³⁴ T. Tomura,⁵⁴ D. Tonelli,⁴⁴ M. Tönnemann,³⁴ S. Torre,⁴⁴ D. Torretta,¹⁵ W. Trischuk,³² R. Tsuchiya,⁵⁶ S. Tsuno,³⁹ D. Tsybychev,¹⁶ N. Turini,⁴⁴ F. Ukegawa,⁵⁴ T. Unverhau,¹⁹ S. Uozumi,⁵⁴ D. Usynin,⁴³ L. Vacavant,²⁸ A. Vaiciulis,⁴⁷ A. Varganov,³³ S. Vejcik III,¹⁵ G. Velez,¹⁵ V. Veszpremi,⁴⁶ G. Veramendi,²³ T. Vickey,²³ R. Vidal,¹⁵ I. Vila,¹⁰ R. Vilar,¹⁰ I. Vollrath,³² I. Volobouev,²⁸ M. von der Mey,⁷ P. Wagner,⁵¹ R.G. Wagner,² R.L. Wagner,¹⁵ W. Wagner,²⁵ R. Wallny,⁷ T. Walter,²⁵ Z. Wan,⁵⁰ M.J. Wang,¹ S.M. Wang,¹⁶ A. Warburton,³² B. Ward,¹⁹ S. Waschke,¹⁹ D. Waters,³⁰ T. Watts,⁵⁰ M. Weber,²⁸ W.C. Wester III,¹⁵ B. Whitehouse,⁵⁵ D. Whiteson,⁴³ A.B. Wicklund,² E. Wicklund,¹⁵ H.H. Williams,⁴³ P. Wilson,¹⁵ B.L. Winer,³⁸ P. Wittich,⁴³ S. Wolbers,¹⁵ C. Wolfe,¹² M. Wolter,⁵⁵ M. Worcester,⁷ S. Worm,⁵⁰ T. Wright,³³ X. Wu,¹⁸ F. Würthwein,⁸ A. Wyatt,³⁰ A. Yagil,¹⁵ T. Yamashita,³⁹ K. Yamamoto,⁴⁰ J. Yamaoka,⁵⁰ C. Yang,⁵⁹ U.K. Yang,¹² W. Yao,²⁸ G.P. Yeh,¹⁵ J. Yoh,¹⁵ K. Yorita,⁵⁶ T. Yoshida,⁴⁰ I. Yu,²⁷ S. Yu,⁴³ J.C. Yun,¹⁵ L. Zanello,⁴⁹ A. Zanetti,⁵³ I. Zaw,²⁰ F. Zetti,⁴⁴ J. Zhou,⁵⁰ and S. Zucchelli,⁴

(CDF Collaboration)

¹ *Institute of Physics, Academia Sinica, Taipei, Taiwan 11529, Republic of China*

² *Argonne National Laboratory, Argonne, Illinois 60439*

³ *Institut de Fisica d'Altes Energies, Universitat Autònoma de Barcelona, E-08193, Bellaterra (Barcelona), Spain*

⁴ *Istituto Nazionale di Fisica Nucleare, University of Bologna, I-40127 Bologna, Italy*

- ⁵ *Brandeis University, Waltham, Massachusetts 02254*
- ⁶ *University of California, Davis, Davis, California 95616*
- ⁷ *University of California, Los Angeles, Los Angeles, California 90024*
- ⁸ *University of California, San Diego, La Jolla, California 92093*
- ⁹ *University of California, Santa Barbara, Santa Barbara, California 93106*
- ¹⁰ *Instituto de Fisica de Cantabria, CSIC-University of Cantabria, 39005 Santander, Spain*
- ¹¹ *Carnegie Mellon University, Pittsburgh, PA 15213*
- ¹² *Enrico Fermi Institute, University of Chicago, Chicago, Illinois 60637*
- ¹³ *Joint Institute for Nuclear Research, RU-141980 Dubna, Russia*
- ¹⁴ *Duke University, Durham, North Carolina 27708*
- ¹⁵ *Fermi National Accelerator Laboratory, Batavia, Illinois 60510*
- ¹⁶ *University of Florida, Gainesville, Florida 32611*
- ¹⁷ *Laboratori Nazionali di Frascati, Istituto Nazionale di Fisica Nucleare, I-00044 Frascati, Italy*
- ¹⁸ *University of Geneva, CH-1211 Geneva 4, Switzerland*
- ¹⁹ *Glasgow University, Glasgow G12 8QQ, United Kingdom*
- ²⁰ *Harvard University, Cambridge, Massachusetts 02138*
- ²¹ *Division of High Energy Physics, Department of Physics, University of Helsinki and Helsinki Institute of Physics, FIN-00014, Helsinki, Finland*
- ²² *Hiroshima University, Higashi-Hiroshima 724, Japan*
- ²³ *University of Illinois, Urbana, Illinois 61801*
- ²⁴ *The Johns Hopkins University, Baltimore, Maryland 21218*
- ²⁵ *Institut für Experimentelle Kernphysik, Universität Karlsruhe, 76128 Karlsruhe, Germany*
- ²⁶ *High Energy Accelerator Research Organization (KEK), Tsukuba, Ibaraki 305, Japan*
- ²⁷ *Center for High Energy Physics: Kyungpook National University, Taegu 702-701; Seoul National University, Seoul 151-742; and SungKyunKwan University, Suwon 440-746; Korea*
- ²⁸ *Ernest Orlando Lawrence Berkeley National Laboratory, Berkeley, California 94720*
- ²⁹ *University of Liverpool, Liverpool L69 7ZE, United Kingdom*
- ³⁰ *University College London, London WC1E 6BT, United Kingdom*
- ³¹ *Massachusetts Institute of Technology, Cambridge, Massachusetts 02139*

³² *Institute of Particle Physics: McGill University, Montréal, Canada H3A 2T8; and University of Toronto, Toronto, Canada M5S 1A7*

³³ *University of Michigan, Ann Arbor, Michigan 48109*

³⁴ *Michigan State University, East Lansing, Michigan 48824*

³⁵ *Institution for Theoretical and Experimental Physics, ITEP, Moscow 117259, Russia*

³⁶ *University of New Mexico, Albuquerque, New Mexico 87131*

³⁷ *Northwestern University, Evanston, Illinois 60208*

³⁸ *The Ohio State University, Columbus, Ohio 43210*

³⁹ *Okayama University, Okayama 700-8530, Japan*

⁴⁰ *Osaka City University, Osaka 588, Japan*

⁴¹ *University of Oxford, Oxford OX1 3RH, United Kingdom*

⁴² *University of Padova, Istituto Nazionale di Fisica Nucleare, Sezione di Padova-Trento, I-35131 Padova, Italy*

⁴³ *University of Pennsylvania, Philadelphia, Pennsylvania 19104*

⁴⁴ *Istituto Nazionale di Fisica Nucleare Pisa, Universities of Pisa, Siena and Scuola Normale Superiore, I-56127 Pisa, Italy*

⁴⁵ *University of Pittsburgh, Pittsburgh, Pennsylvania 15260*

⁴⁶ *Purdue University, West Lafayette, Indiana 47907*

⁴⁷ *University of Rochester, Rochester, New York 14627*

⁴⁸ *The Rockefeller University, New York, New York 10021*

⁴⁹ *Istituto Nazionale di Fisica Nucleare, Sezione di Roma 1, University di Roma "La Sapienza," I-00185 Roma, Italy*

⁵⁰ *Rutgers University, Piscataway, New Jersey 08855*

⁵¹ *Texas A&M University, College Station, Texas 77843*

⁵² *Texas Tech University, Lubbock, Texas 79409*

⁵³ *Istituto Nazionale di Fisica Nucleare, University of Trieste/ Udine, Italy*

⁵⁴ *University of Tsukuba, Tsukuba, Ibaraki 305, Japan*

⁵⁵ *Tufts University, Medford, Massachusetts 02155*

⁵⁶ *Waseda University, Tokyo 169, Japan*

⁵⁷ *Wayne State University, Detroit, Michigan 48201*

⁵⁸ *University of Wisconsin, Madison, Wisconsin 53706*

⁵⁹ *Yale University, New Haven, Connecticut 06520*

We report on a study of jet shapes in inclusive jet production in $p\bar{p}$ collisions at $\sqrt{s} = 1.96$ TeV

using the upgraded Collider Detector at Fermilab in Run II (CDF II) based on an integrated luminosity of 170 pb^{-1} . Measurements are carried out on jets with rapidity $0.1 < |Y^{\text{jet}}| < 0.7$ and transverse momentum $37 \text{ GeV}/c < P_T^{\text{jet}} < 380 \text{ GeV}/c$. The jets have been corrected to the hadron level. The measured jet shapes are compared to leading-order QCD parton-shower Monte Carlo predictions as implemented in the PYTHIA and HERWIG programs. PYTHIA, tuned to describe the underlying event as measured in CDF Run I, provides a better description of the measured jet shapes than does PYTHIA or HERWIG with their default parameters.

PACS numbers: 13.85.Ni, 13.85.Qk, 14.65.Ha, 87.18.Sn

I. INTRODUCTION

The measurement of the jet shape allows a study of the transition between a parton produced in a hard process and the collimated flow of hadrons observed experimentally [1]. The internal structure of a jet is dominated by multi-gluon emissions from the primary outgoing parton and is expected to depend mainly on the type of parton, quark or gluon, creating the jet and the transverse momentum of the jet. In hadron-hadron collisions, the jet shape also receives contributions from initial-state radiation emitted from the colliding partons and multiple parton interactions between remnants (the so-called *underlying event*). The effects of initial-state radiation are described by the parton showering in QCD Monte Carlo programs while the underlying event description is provided by phenomenological models. The comparison of jet cross section measurements with perturbative QCD predictions, as well as the estimation of QCD backgrounds in the search for new physics, requires an accurate description of the underlying event. The study of jet shapes at the Tevatron provides a precise means to test the validity of the models for parton cascades and the underlying event in hadron-hadron collisions. Measurements of the jet shape have been performed in $p\bar{p}$ collisions at $\sqrt{s} = 1.8 \text{ TeV}$ [2], deeply inelastic scattering (DIS) [3] and photoproduction [4] processes in $e^\pm p$ collisions at HERA, and e^+e^- interactions at LEP1 [5]. It was observed [5] that the jets in $p\bar{p}$ collisions are significantly broader than those in e^+e^- with most of the difference being explained in terms of the different mixtures of quark and gluon jets in the final state. The jets in DIS were found to be very similar to those in e^+e^- interactions and narrower than those in $p\bar{p}$ collisions. In this paper, new jet shape results in $p\bar{p}$ collisions, based on CDF Run II data, are presented for central jets in a wide range in jet transverse momentum. For the first time, these measurements extend the study of the jet internal structure to jets with transverse momentum up to $380 \text{ GeV}/c$.

II. EXPERIMENTAL SETUP

The CDF II detector is described in detail in [6]. In this section, the sub-detectors most relevant for this analysis are briefly discussed. As illustrated in Fig. 1, the detector has a charged particle tracking system immersed in a 1.4 T magnetic field, aligned coaxially with the beam line. A silicon microstrip detector [7] provides tracking over the radial range 1.35 to 28 cm. A 3.1 m long open-cell drift chamber, the Central Outer Tracker (COT) [8], covers the radial range from 44 to 132 cm. The fiducial region of the silicon detector covers the pseudorapidity [9] range $|\eta| \leq 2$, while the COT provides coverage for $|\eta| \leq 1$. The charged particles are reconstructed in the COT with a transverse-momentum resolution of $\sigma(p_T)/p_T^2 \sim 1.7 \cdot 10^{-3} [\text{GeV}/c]^{-1}$. Segmented sampling calorimeters, arranged in a projective tower geometry, surround the tracking system and measure the energy flow of interacting particles in $|\eta| \leq 3.6$. The CDF central barrel calorimeter [10] is unchanged from Run I and covers the region $|\eta| < 1$. It consists of an electromagnetic (CEM) calorimeter and an hadronic (CHA) calorimeter segmented into 480 towers of size 0.1 in η and 15° in ϕ . The end-wall hadronic (WHA) calorimeter [11] complements the coverage of the central barrel calorimeter in the region $0.6 < |\eta| < 1.0$ and provides additional forward coverage out to $|\eta| < 1.3$. In Run II, new forward scintillator-plate calorimeters [12] replaced the original Run I gas calorimeter system. The new plug electromagnetic (PEM) calorimeter covers the region $1.1 < |\eta| < 3.6$ while the new hadronic (PHA) calorimeter provides coverage in the $1.3 < |\eta| < 3.6$ region. Each plug calorimeter is segmented into 480 towers with sizes that vary as a function of η (0.1 in η and 7.5° in ϕ for $|\eta| < 1.8$ to 0.6 in η and 15° in ϕ at $|\eta| = 3.6$). The calorimetry has a crack at $\eta = 0$ (between the two halves of the central barrel calorimeter) and two cracks at $\eta = \pm 1.1$ (in the region between the WHA and the plug calorimeters). The measured energy resolutions for electrons in the electromagnetic calorimeters are $14\%/\sqrt{E_T}$ (CEM) and $16\%/\sqrt{E} \oplus 1\%$ (PEM) where the units are expressed in GeV. The single-pion energy resolutions in the hadronic calorimeters, as determined in test-beam data, are $75\%/\sqrt{E_T}$ (CHA), $80\%/\sqrt{E}$ (WHA) and $80\%/\sqrt{E} \oplus 5\%$ (PHA). Cherenkov counters located in the $3.7 < |\eta| < 4.7$ region [13] measure the average number of inelastic $p\bar{p}$ collisions per bunch crossing and thereby determine the beam luminosity. Finally, a three-level trigger system [14] is used to select events online, as described in section V.

III. MONTE CARLO SIMULATION

Monte Carlo event samples are used to determine the response of the detector and the correction factors to the hadron level [15] for the measured jet shapes. The generated samples are passed through a full CDF detector

simulation (based on GEANT3 [16] where the GFLASH [17] package is used to simulate the energy deposition in the calorimeters), and then reconstructed and analyzed using the same analysis chain as in the data. Samples of simulated inclusive jet events have been generated using the PYTHIA 6.203 [18] and HERWIG 6.4 [19] Monte Carlo generators. In both programs, the partonic interactions are generated using leading-order QCD matrix elements, including initial- and final-state parton showers. CTEQ5L [20] parton distribution functions are used for the proton and antiproton. The HERWIG samples have been generated using default parameters. The PYTHIA samples have been created using a special tuned set of parameters, denoted as PYTHIA-Tune A [21], that includes enhanced contributions from initial-state gluon radiation and secondary parton interactions between remnants. Tune A was determined as a result of dedicated studies of the underlying event in dijet events performed using the CDF Run I data [22]. In addition, two different PYTHIA samples have been generated using the default parameters with and without the contribution from multiple parton interactions (MPI) between the proton and antiproton remnants. The latter are denoted as PYTHIA-(no MPI). The HERWIG samples do not include multiple parton interactions. Fragmentation into hadrons is carried out using the string model [23] as implemented in JETSET [24] in the case of PYTHIA and the cluster model [25] in HERWIG.

IV. JET RECONSTRUCTION

An iterative cone-based midpoint algorithm [26] in the Y - ϕ plane [9] is used to reconstruct jets from the energy deposits in the calorimeter towers for both data and the Monte Carlo simulated events, and from final-state particles for the Monte Carlo generated events. This procedure is explained in detail below for the jet reconstruction from the calorimeter towers. In the first step, the electromagnetic and hadronic sections of each calorimeter tower are preclustered into a *physics* tower. The position of each section is determined from the unit vector joining the vertex of the interaction and the section's geometrical center. Each section is assumed to be massless. The four-vector components of each *physics* tower are then computed using the four-momentum sum of its electromagnetic and hadronic sections; only towers with transverse momentum above 0.1 GeV/c are further considered. In a second step, each *physics* tower with transverse momentum above 1 GeV/c is used to define a seed for the jet search. Starting from the seed with highest transverse momentum, a cone is drawn around each seed and the *physics* towers inside a distance $\sqrt{(\Delta Y)^2 + (\Delta \phi)^2} < R/2$, with $R = 0.7$ are used to determine the direction of the new cluster as indicated

in Eqs. 1 and 2:

$$E^{\text{cluster}} = \sum_{\text{phys.towers}} E^{\text{tower}}, \quad P_i^{\text{cluster}} = \sum_{\text{phys.towers}} P_i^{\text{tower}} \quad i = x, y, z \quad (1)$$

$$P_T^{\text{cluster}} = \sqrt{(P_x^{\text{cluster}})^2 + (P_y^{\text{cluster}})^2}, \quad Y^{\text{cluster}} = \frac{1}{2} \frac{E^{\text{cluster}} + P_z^{\text{cluster}}}{E^{\text{cluster}} - P_z^{\text{cluster}}}, \quad \phi^{\text{cluster}} = \tan^{-1} \left(\frac{P_y^{\text{cluster}}}{P_x^{\text{cluster}}} \right) \quad (2)$$

where Y^{cluster} and ϕ^{cluster} denote the rapidity and azimuthal angle of the cluster, respectively. Starting from the list of resulting clusters, the procedure is iterated until the contents of the clusters remain unchanged. In a third step, the midpoint (Y - ϕ plane) between each pair of stable clusters separated by less than $2R$ is added to the list of clusters. The clustering algorithm, as explained above, is again iterated until stability is achieved. This latter step gives the name to the jet algorithm and was introduced in order to address the theoretical difficulties [27] of the cone-based jet algorithm used in Run I [28]. Finally, the cone size is expanded from $R/2$ to R [26] and the momentum sharing of overlapping clusters is considered. Overlapping jets are merged if their shared momentum is larger than 75% of the jet with smaller transverse momentum; otherwise two jets are formed and the common towers are assigned to the nearest jet. The variables for jets reconstructed from the calorimeter towers are denoted by $P_{T,\text{CAL}}^{\text{jet}}$, $Y_{\text{CAL}}^{\text{jet}}$ and $\phi_{\text{CAL}}^{\text{jet}}$. As mentioned, the same jet algorithm is applied to the final-state hadrons in Monte Carlo generated events. In this case, the four-vector components of each individual hadron are used as input to the algorithm and no cut on the minimum transverse momentum of the particles is applied. The variables of the hadron-level jets are denoted by $P_{T,\text{HAD}}^{\text{jet}}$, $Y_{\text{HAD}}^{\text{jet}}$ and $\phi_{\text{HAD}}^{\text{jet}}$.

The reconstruction of the jet variables in the calorimeter is studied using Monte Carlo event samples and matched pair of jets at the calorimeter and hadron levels. These studies indicate that the angular variables of the jet, $Y_{\text{CAL}}^{\text{jet}}$ and $\phi_{\text{CAL}}^{\text{jet}}$, are reconstructed in the calorimeter with no significant systematic shift and with a resolution, for jets with $P_{T,\text{CAL}}^{\text{jet}} > 20$ GeV/c, of the order of 0.02 units and 0.025 units, respectively. The resolutions improve as the measured jet transverse momentum increases. The jet transverse momentum measured in the calorimeter, $P_{T,\text{CAL}}^{\text{jet}}$, systematically underestimates that of the hadron level jet. This is mainly due to the non-compensating nature of the calorimeter [29]. For jets with $P_{T,\text{CAL}}^{\text{jet}} > 20$ GeV/c the jet transverse momentum is reconstructed with an average shift of -20% and an r.m.s of 17% . The reconstruction of the jet transverse momentum improves as $P_{T,\text{CAL}}^{\text{jet}}$ increases.

For jets with $P_{T,CAL}^{\text{jet}} > 130 \text{ GeV}/c$ the jet transverse momentum is reconstructed with an average shift of -12% and an r.m.s of 9% . An average correction is extracted from the Monte Carlo using the following procedure: matched pairs of jets are used to study the difference between the jet transverse momentum at the hadron level, $P_{T,HAD}^{\text{jet}}$, and the corresponding measurement in the calorimeter, $P_{T,CAL}^{\text{jet}}$. The resulting correlation is used to extract multiplicative correction factors, $C(P_{T,CAL}^{\text{jet}})$, which are then applied to the measured jets to obtain the corrected jet transverse momenta, $P_{T,COR}^{\text{jet}} = C \times P_{T,CAL}^{\text{jet}}$ [30].

V. EVENT SELECTION

This analysis is based on a sample of inclusive jet events selected from the CDF Run II data corresponding to a total integrated luminosity of 170 pb^{-1} . Events were collected *online* using three-level trigger paths, based on the measured energy deposits in the calorimeter towers, with several different thresholds on the jet transverse energies. In the first-level trigger, a single trigger tower with transverse energy above 5 GeV or 10 GeV , depending on the trigger path, is required. In the second-level trigger, a hardware-based clustering is carried out where calorimeter clusters are formed around the selected trigger towers. The events are required to have at least one second-level trigger cluster with transverse energy above a given threshold, which varies between 15 and 90 GeV for the different trigger paths. In the third-level trigger, jets are reconstructed using the CDF Run I cone algorithm [28] and the events are required to have at least one jet with transverse energy above 20 to 100 GeV depending on the trigger path. Offline, jets are reconstructed using the midpoint algorithm, as explained above, starting from seed calorimeter towers with transverse momentum above $1 \text{ GeV}/c$ and only considering towers with a minimum transverse momentum of $100 \text{ MeV}/c$ in the clustering procedure. The following selection criteria have been imposed:

- One reconstructed primary vertex with z -component, V_Z , in the region $|V_Z| < 60 \text{ cm}$. Events with more than one primary vertex are removed to eliminate contributions from pile-up events with multiple proton-antiproton interactions per beam crossing. The data used in this study was collected at Tevatron instantaneous luminosities in the range between $0.2 \times 10^{31} \text{ cm}^{-2} \text{ s}^{-1}$ and $4 \times 10^{31} \text{ cm}^{-2} \text{ s}^{-1}$ for which, on average, less than one interaction per crossing is expected.
- $\cancel{E}_T / \sqrt{E_T} < 3.5 \text{ GeV}^{1/2}$, where \cancel{E}_T (E_T) denotes the missing (total) transverse energy of the event as determined from the energy deposits in the calorimeter towers. This cut eliminates beam-related backgrounds, beam halo and beam-gas contributions, and cosmic rays.

- At least one jet with $P_{T,\text{COR}}^{\text{jet}} > 37 \text{ GeV}/c$ and Y^{jet} in the region $0.1 < |Y^{\text{jet}}| < 0.7$.

The cut on the minimum $P_{T,\text{COR}}^{\text{jet}}$ is dictated by the trigger. In order to avoid any possible bias on the measured jet shapes due to the three-level trigger selection, the thresholds on $P_{T,\text{COR}}^{\text{jet}}$, applied to the different data samples, have been selected such that the trigger is fully efficient in the whole kinematic region under study. The measurements are performed for central jets in a rapidity region away from calorimeter cracks and inside the fiducial region of the CDF tracking system.

VI. JET SHAPE

A. Jet shape definition

The differential jet shape as a function of the distance $r = \sqrt{\Delta Y^2 + \Delta\phi^2}$ to the jet axis, $\rho(r)$, is defined as the average fraction of the jet transverse momentum that lies inside an annulus of inner radius $r - \delta r/2$ and outer radius $r + \delta r/2$ around the jet:

$$\rho(r) = \frac{1}{\delta r} \frac{1}{N_{\text{jet}}} \sum_{\text{jets}} \frac{P_T(r - \delta r/2, r + \delta r/2)}{P_T(0, R)}, \quad 0 \leq r \leq R \quad (3)$$

where N_{jet} denotes the total number of jets, $P_T(r - \delta r/2, r + \delta r/2)$ is the transverse momentum within an annulus and the jet shape is determined for values of r between 0.05 and 0.65 using $\delta r = 0.1$ intervals. The points from the differential jet shape at different r values are correlated since, by definition, $\int_0^R \rho(r) \delta r = 1$.

The integrated jet shape, $\Psi(r)$, is defined as the average fraction of the jet transverse momentum that lies inside a cone of radius r concentric to the jet cone:

$$\Psi(r) = \frac{1}{N_{\text{jet}}} \sum_{\text{jets}} \frac{P_T(0, r)}{P_T(0, R)}, \quad 0 \leq r \leq R \quad (4)$$

where, by definition, $\Psi(r = R) = 1$. The integrated jet shape is determined in intervals $\delta r = 0.1$ between $r = 0$ and $r = 0.7$, and the points at different r values are strongly correlated.

B. Jet shape reconstruction

Calorimeter towers are used for both data and Monte Carlo simulated events to reconstruct the differential jet shape. For each jet, the scalar sum of the transverse momentum of the calorimeter towers assigned to it, $P_T(r - \delta r/2, r + \delta r/2)$, with a distance to the jet axis $r' = \sqrt{(Y^{\text{tower}} - Y^{\text{jet}})^2 + (\phi^{\text{tower}} - \phi^{\text{jet}})^2}$ between $r - \delta r/2$ and $r + \delta r/2$, is determined and divided by $P_T(0, R)$. The differential jet shape, $\rho^{\text{CAL}}(r)$, is then determined following the prescription in Eq. 3. Similarly, the integrated jet shape, $\Psi^{\text{CAL}}(r)$, is reconstructed using the calorimeter towers as defined in Eq. 4. The same procedure is applied to the final-state particles in Monte Carlo generated events to reconstruct the differential and integrated jet shapes at the hadron level, $\rho_{\text{MC}}^{\text{HAD}}(r)$ and $\Psi_{\text{MC}}^{\text{HAD}}(r)$, respectively. In the case of hadron-level jets no grid in the $(Y-\phi)$ space has been used.

C. Jet shape using charged particles

The CDF tracking system provides an alternative method to measure the shape of the jets using charged particles. For each jet, tracks with transverse momentum, p_T^{track} , above 0.5 GeV/c and pseudorapidity, η^{track} , in the region $|\eta^{\text{track}}| < 1.4$ are assigned to it if their distances, r , with respect to the jet axis are smaller than 0.7, and the tracks project to within 2 cm of the z -position of the primary vertex. The differential and integrated jet shapes, $\rho^{\text{TRKS}}(r)$ and $\Psi^{\text{TRKS}}(r)$, are then reconstructed using the track information and following Eqs. 3 and 4. The measured jet shapes using tracks are employed to study systematic uncertainties on the central measurements as determined using calorimeter towers (see next section). Therefore, detailed studies have been performed on track reconstruction efficiency inside jets as a function of r and the jet and track transverse momenta, for both data and simulated events, using track embedding techniques [31]. The difference between efficiencies in the data and Monte Carlo are about 3%, and approximately independent of r for tracks with $0.5 \text{ GeV}/c < p_T^{\text{track}} < 2.0 \text{ GeV}/c$. For tracks with $p_T^{\text{track}} > 2.0 \text{ GeV}/c$, the difference in efficiency is of the order of 5% at the core of the jet, decreasing as r increases up to $r = 0.5$. For $r > 0.5$ no difference in efficiency is observed. The effect on the reconstructed jet shapes is smaller than 0.5% and thus has been absorbed into the systematic error.

VII. UNFOLDING AND SYSTEMATIC STUDIES

The measured jet shapes, as determined using calorimeter towers, are corrected back to the hadron level using Monte Carlo samples of generated events. PYTHIA-Tune A provides a good description of the measured jet shapes

in all regions of P_T^{jet} and is used to determine the correction factors in the unfolding procedure.

A. Jet shape corrections

The measured jet shapes are corrected for acceptance and smearing effects back to the hadron level. The correction factors also account for the efficiency of the selection criteria and for jet reconstruction in the calorimeter. Differential and integrated jet shapes are reconstructed with Monte Carlo samples using both calorimeter towers, $\rho_{\text{MC}}^{\text{CAL}}(r)$ and $\Psi_{\text{MC}}^{\text{CAL}}(r)$, and final-state particles, $\rho_{\text{MC}}^{\text{HAD}}(r)$ and $\Psi_{\text{MC}}^{\text{HAD}}(r)$, in different regions of $P_{T,\text{COR}}^{\text{jet}}$ and $P_{T,\text{HAD}}^{\text{jet}}$, respectively. Correction factors, defined as $D(r) = \rho_{\text{MC}}^{\text{HAD}}(r)/\rho_{\text{MC}}^{\text{CAL}}(r)$ and $I(r) = \Psi_{\text{MC}}^{\text{HAD}}(r)/\Psi_{\text{MC}}^{\text{CAL}}(r)$, are then computed separately in each bin of $P_{T,\text{COR}}^{\text{jet}}$. The corrected differential and integrated measurements are determined from the measured jet shapes as $\rho(r) = D(r) \cdot \rho^{\text{CAL}}(r)$ and $\Psi(r) = I(r) \cdot \Psi^{\text{CAL}}(r)$. The correction factors $D(r)$ do not show a significant dependence on P_T^{jet} and vary between 1.2 and 0.9 as r increases. For the integrated jet shapes, the correction factors $I(r)$ differ from unity by less than 10% for $r > 0.2$.

B. Systematic uncertainties

A detailed study of the different sources of systematic uncertainties on the measured jet shapes has been performed [30]:

- The measured jet transverse momentum has been varied by $\pm 5\%$ in the data to account for the uncertainty on the determination of the absolute energy scale in the calorimeter. The effect on the measured jet shapes is of the order of 2%.
- The unfolding procedure has been repeated using bin-by-bin correction factors extracted from HERWIG instead of PYTHIA-Tune A to account for any possible dependence on the modeling of parton cascades. The effect on the measured jet shapes is about 2% to 5%.
- The ratios of uncorrected jet shape measurements as determined using calorimeter towers and tracks, $\rho^{\text{CAL}}(r)/\rho^{\text{TRKS}}(r)$ and $\Psi^{\text{CAL}}(r)/\Psi^{\text{TRKS}}(r)$, are compared between data and Monte Carlo simulated events. The deviations from unity observed in the data/Monte Carlo double ratio, below 5% for the whole P_T^{jet} range, are included in the systematic errors to account for the uncertainty on the description of the inactive material in front of the calorimeter and its response to low-energy particles.

- The measurements are performed in different periods of Tevatron instantaneous luminosity (between $0.2 \cdot 10^{31} \text{ cm}^{-2}\text{s}^{-1}$ and $4 \cdot 10^{31} \text{ cm}^{-2}\text{s}^{-1}$) to account for possible remaining contributions from pile-up events. No significant effect is found.

The total systematic uncertainties on $\rho(r)$ and $\Psi(r)$ have been computed for the different r ranges by adding in quadrature the deviations from the central values. The statistical uncertainties are negligible compared to the systematic errors except for jets with $P_T^{\text{jet}} > 300 \text{ GeV}/c$. The systematic uncertainties have been added in quadrature to the statistical errors and the total uncertainties are shown in the figures. The total uncertainty in the measured data points, for different P_T^{jet} and r ranges, varies between 5% to 10% except for jets with $P_T^{\text{jet}} > 300 \text{ GeV}/c$ for which the total error is above 20%.

VIII. RESULTS

The corrected differential and integrated jet shapes, $\rho(r)$ and $\Psi(r)$, refer to midpoint jets at the hadron level with cone size $R = 0.7$ in the region $0.1 < |Y^{\text{jet}}| < 0.7$ and $37 \text{ GeV}/c < P_T^{\text{jet}} < 380 \text{ GeV}/c$.

A. Comparison with Monte Carlo

Figures 2 and 3 show the measured differential jet shapes, $\rho(r/R)$, in bins of P_T^{jet} for jets in the region $0.1 < |Y^{\text{jet}}| < 0.7$ and $37 \text{ GeV}/c < P_T^{\text{jet}} < 380 \text{ GeV}/c$, compared to the PYTHIA-Tune A and HERWIG Monte Carlo predictions at the hadron level. The measured jet shapes show a prominent peak at low r which indicates that the majority of the jet momentum is concentrated at $r/R < 0.2$. At low P_T^{jet} , the fraction of transverse momentum at the core of the jet is about a factor of 6 times larger than that at the tail. This factor increases at higher P_T^{jet} and is of the order of 100 for jets with $P_T^{\text{jet}} > 340 \text{ GeV}/c$. PYTHIA-Tune A provides a good description of the measured jet shapes in all regions of P_T^{jet} . The jets predicted by HERWIG follow the measurements but tend to be narrower than the data at low P_T^{jet} . The latter can be attributed to the absence of additional soft contributions from multiple parton interactions in HERWIG, which are particularly important at low P_T^{jet} .

Figures 4 and 5 present the measured integrated jet shapes, $\Psi(r/R)$, in bins of P_T^{jet} , for jets with $0.1 < |Y^{\text{jet}}| < 0.7$ and $37 \text{ GeV}/c < P_T^{\text{jet}} < 380 \text{ GeV}/c$, compared to HERWIG, PYTHIA-Tune A, PYTHIA and PYTHIA-(no MPI) predictions, to illustrate the importance of a proper modeling of soft-gluon radiation in describing the measured jet shapes. In addition, Figure 6 shows, for a fixed radius $r_0 = 0.3$, the average fraction of the jet transverse momentum

outside $r = r_0$, $(1 - \Psi(r_0/R))$, as a function of P_T^{jet} . The points are located at the weighted mean in each P_T^{jet} range. The measurements show that the fraction of jet transverse momentum inside a given fixed r_0/R increases ($1 - \Psi(r_0/R)$ decreases) with P_T^{jet} , indicating that the jets become narrower as P_T^{jet} increases. PYTHIA with default parameters produces jets systematically narrower than the data in the whole region in P_T^{jet} . The contribution from secondary parton interactions between remnants to the predicted jet shapes (as shown by the difference between PYTHIA and PYTHIA-(no MPI) predictions) is important at low P_T^{jet} . PYTHIA-Tune A predictions describe all of the data well (a χ^2 test in Fig. 6 gives a value of 13.6 for a total of 18 data points). HERWIG describes the measured jet shapes well but produces jets slightly narrower than the data at low P_T^{jet} . This results in a significantly higher χ^2 value of 33.8 for 18 data points.

B. Quark- and gluon-jet contributions

Figures 7 and 8 present the measured integrated jet shapes, $\Psi(r/R)$, in bins of P_T^{jet} , for jets with $0.1 < |Y^{\text{jet}}| < 0.7$ and $37 \text{ GeV}/c < P_T^{\text{jet}} < 380 \text{ GeV}/c$, compared to PYTHIA-Tune A predictions (as in Figs. 4 and 5). In these figures, predictions are also shown separately for quark- and gluon-jets. Each hadron-level jet from PYTHIA is classified as a quark- or gluon-jet by matching (Y - ϕ plane) its direction with that of one of the outgoing partons from the hard interaction. The Monte Carlo predictions indicate that, for the jets used in this analysis, the measured jet shapes are dominated by contributions from gluon-initiated jets at low P_T^{jet} while contributions from quark-initiated jets become important at high P_T^{jet} . This can be explained in terms of the different partonic contents in the proton and antiproton contributing to the low- and high- P_T^{jet} regions, since the mixture of gluon- and quark-jet in the final state partially reflects the nature of the incoming partons that participate in the hard interaction. Figure 9 shows the measured $1 - \Psi(r_0/R)$, $r_0 = 0.3$, as a function of P_T^{jet} compared to PYTHIA-Tune A predictions with quark- and gluon-jets shown separately. The trend with P_T^{jet} in the measured jet shapes is mainly attributed to the different quark- and gluon-jet mixture in the final state and perturbative QCD effects related to the running of the strong coupling, $\alpha_s(P_T^{\text{jet}})$.

IX. SUMMARY AND CONCLUSIONS

Jet shapes have been measured in inclusive jet production in $p\bar{p}$ collisions for jets in the kinematic region $37 \text{ GeV}/c < P_T^{\text{jet}} < 380 \text{ GeV}/c$ and $0.1 < |Y^{\text{jet}}| < 0.7$. Jets become narrower as P_T^{jet} increases which can be mainly attributed to the

change in the quark- and gluon-jet mixture in the final state and the running of the strong coupling with P_T^{jet} . PYTHIA Monte Carlo predictions, using default parameters, do not give a good description of the measured jet shapes in the entire P_T^{jet} range. PYTHIA-Tune A, which includes enhanced contributions from initial-state gluon radiation and secondary parton interactions between remnants, describes the data better. HERWIG gives a reasonable description of the measured jet shapes but tends to produce jets that are too narrow at low P_T^{jet} which can be attributed to the absence of soft contributions from multiple parton interactions in HERWIG. Jet shape measurements thus can be used to introduce strong constraints on phenomenological models describing soft-gluon radiation and the underlying event in hadron-hadron interactions.

Acknowledgments

We thank the Fermilab staff and the technical staffs of the participating institutions for their vital contributions. This work was supported by the U.S. Department of Energy and National Science Foundation; the Italian Istituto Nazionale di Fisica Nucleare; the Ministry of Education, Culture, Sports, Science and Technology of Japan; the Natural Sciences and Engineering Research Council of Canada; the National Science Council of the Republic of China; the Swiss National Science Foundation; the A.P. Sloan Foundation; the Bundesministerium fuer Bildung und Forschung, Germany; the Korean Science and Engineering Foundation and the Korean Research Foundation; the Particle Physics and Astronomy Research Council and the Royal Society, UK; the Russian Foundation for Basic Research; the Comision Interministerial de Ciencia y Tecnologia, Spain; in part by the European Community's Human Potential Programme under contract HPRN-CT-2002-00292; and the Academy of Finland.

-
- [1] S.D.Ellis, Z. Kunszt and D.E. Soper, Phys. Rev. Lett. **69**, 3615 (1992).
 - [2] CDF Collab., F. Abe et al., Phys. Rev. Lett. **70**, 713 (1993).
D0 Collab., S. Abachi et al., Phys. Lett. B **357**, 500 (1995).
 - [3] ZEUS Collab., J. Breitweg et al., The Eur. Phys. Journal C **8**, 3 367-380 (1999).
H1 Collab., C. Adloff et al., Nucl. Phys. B **545**, 3-20 (1999).
 - [4] ZEUS Collab., J. Breitweg et al., The Eur. Phys. Journal C **2**, 1 61-75 (1998).
 - [5] OPAL Collab., R. Akers et al., Zeit. f. Phys. C **63**, 197 (1994).
 - [6] CDF II Collab., FERMILAB-PUB-96/390-E (1996).
D. Acosta et al., Phys. Rev. D **71**, 032001 (2005).

- [7] A. Sill et al., Nucl. Instrum. Meth. A **447**, 1 (2000).
 A. Affolder et al., Nucl. Instrum. Meth. A **453**, 84 (2000).
 C.S. Hill, Nucl. Instrum. Meth. A **530**, 1 (2000).
- [8] T. Affolder et al., Nucl. Instrum. Meth. A **526**, 249 (2004).
- [9] The pseudorapidity is defined as $\eta = -\ln(\tan(\frac{\theta}{2}))$, where the polar angle θ is taken with respect to the proton beam direction. The rapidity is defined as $Y = \frac{1}{2}\ln(\frac{E+p_z}{E-p_z})$, where E denotes the energy and p_z is the component of the momentum along the proton beam direction.
- [10] L. Balka et al., Nucl. Instr. Meth. A **267**, 272 (1988).
- [11] S. Bertolucci et al., Nucl. Instr. Meth. A **267**, 301 (1988).
- [12] R. Oishi, Nucl. Instr. Meth. A **453**, 277 (2000).
 M. G. Albrow et al., Nucl. Instr. Meth. A **480**, 524 (2002).
- [13] D. Acosta et al., Nucl. Instrum. Meth., A **494**, 57 (2002).
- [14] B. L. Winer, Int. J. Mod. Phys. A **A16S1C**, 1169 (2001).
- [15] The hadronic final state in the Monte Carlo generators is defined using particles with lifetime above 10^{-11} s.
- [16] R. Brun et al., Technical Report CERN-DD/EE/84-1, CERN, 1987.
- [17] G. Grindhammer, M. Rudowicz and S. Peters, Nucl. Instrum. Meth. A **290** 469 (1990).
- [18] T. Sjöstrand et al., Comp. Phys. Comm. **135**, 238 (2001) [arXiv:hep-ph/0010017 (2000)].
- [19] G. Corcella et al., JHEP **0101**, 010 (2001) [arXiv:hep-ph/0011363 (2000)]; arXiv:hep-ph/0210213 (2002).
- [20] J. Pumplin et al., JHEP **0207** 012 (2002).
- [21] PYTHIA-Tune A Monte Carlo samples are generated using the following tuned parameters in PYTHIA: PARP(67) = 4.0, MSTP(82) = 4, PARP(82) = 2.0, PARP(84) = 0.4, PARP(85) = 0.9, PARP(86) = 0.95, PARP(89) = 1800.0, PARP(90) = 0.25.
- [22] D. Acosta et al., CDF Collaboration, Phys. Rev. D **65**, 092002 (2002).
- [23] B. Andersson et al., Phys. Rep. **97**, 31 (1983).
- [24] T. Sjöstrand, Comp. Phys. Comm. **39**, 347 (1986).
- [25] B.R. Webber, Nucl. Phys. B **238**, 492 (1984).
- [26] G. C. Blazey, et al., arXiv:hep-ex/0005012 (2000).
 S.D. Ellis, J. Huston and M. Toennesmann, arXiv:hep-ph/0111434 (2001).
- [27] M. H. Seymour, Nucl.Phys. B **513**, 269 (1998).
- [28] CDF Collab., F. Abe et al., Phys. Rev. D **45**, 1448 (1992).
- [29] S.R. Hahn, et al., NIM A **267**, 351 (1988).
- [30] Olga Norriella, PhD. Thesis, Universitat Autònoma de Barcelona, in preparation.

[31] Simon Sabik, PhD. Thesis, University of Toronto, in preparation.

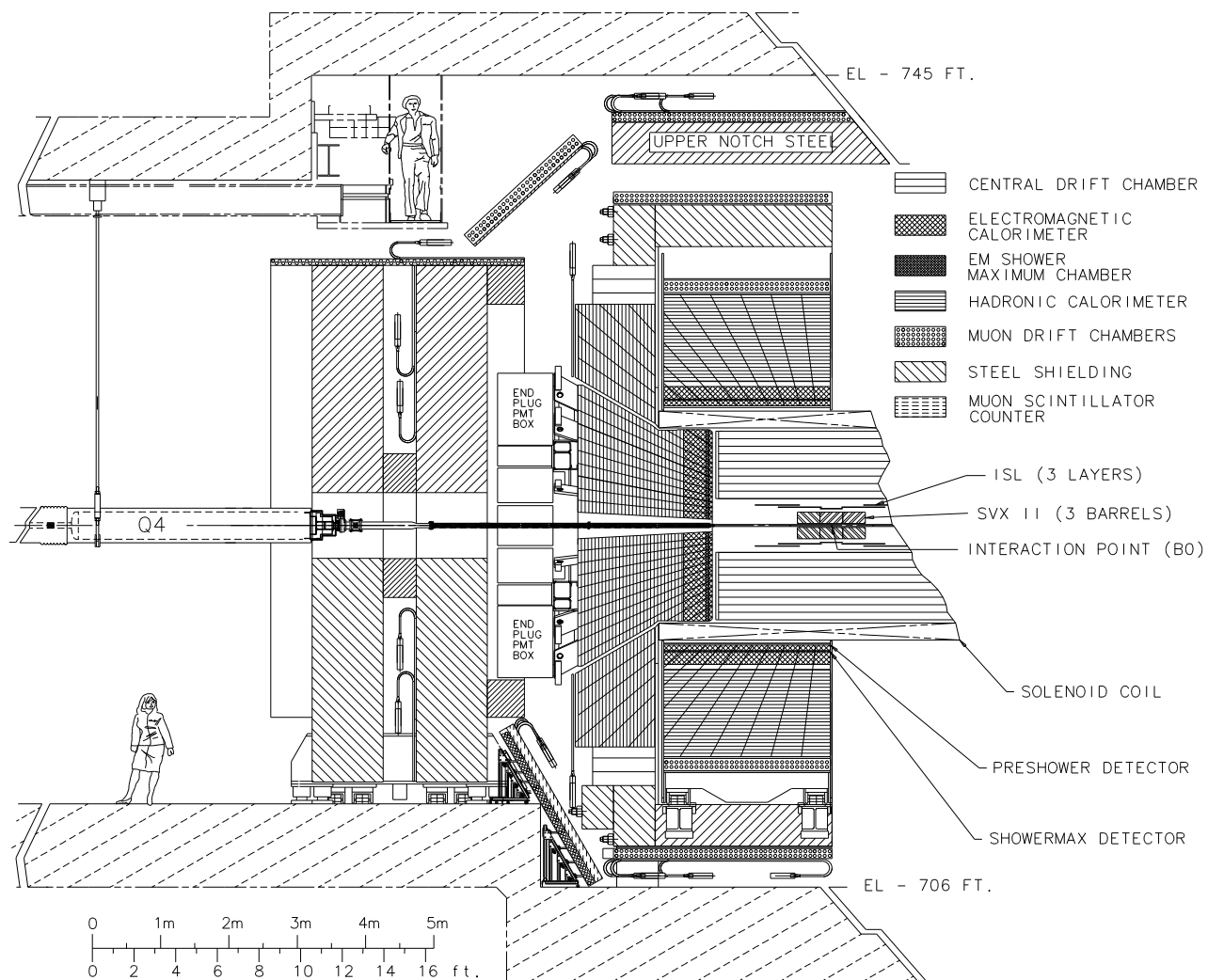


FIG. 1: Longitudinal view of half of the CDF II detector.

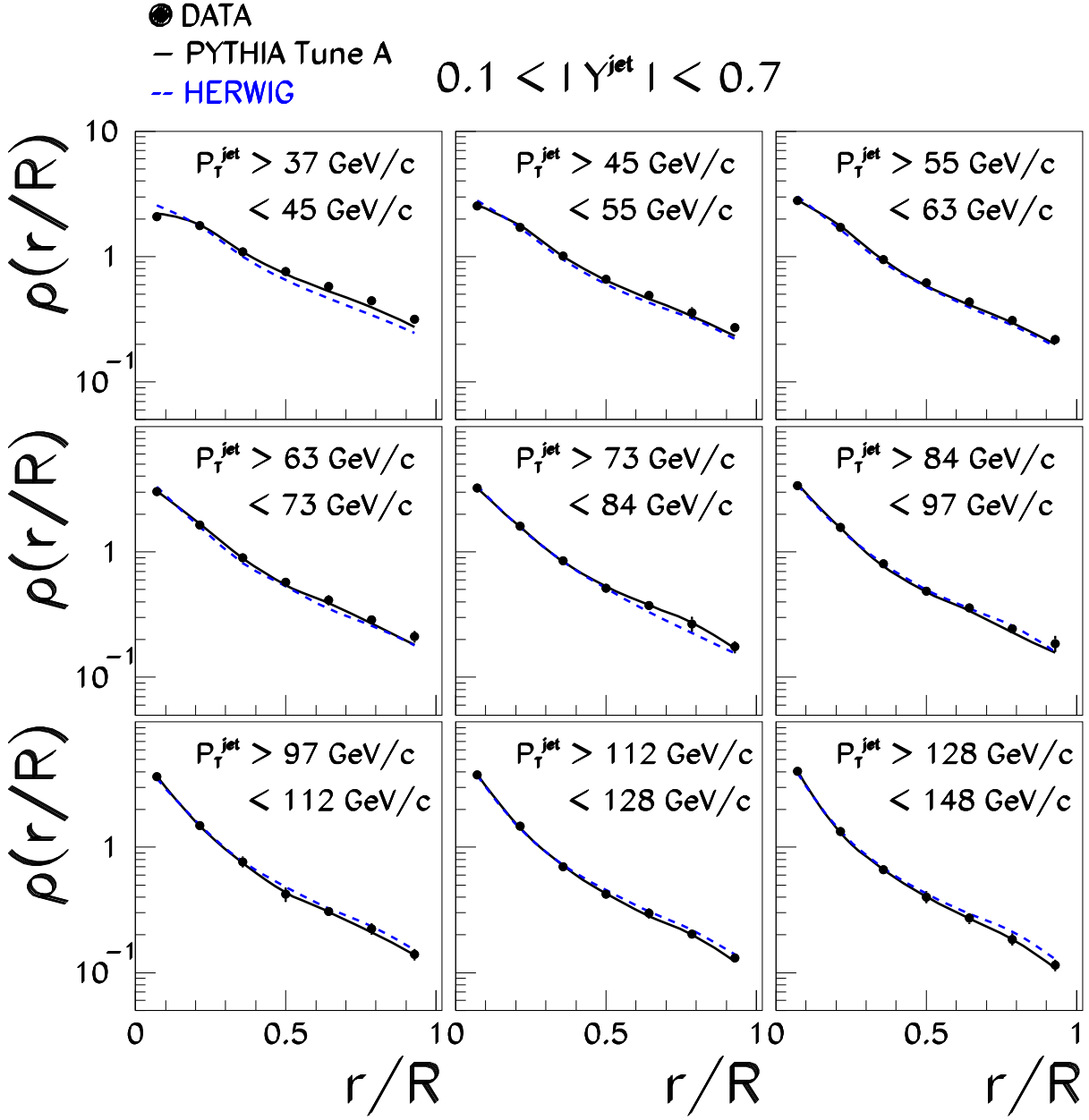


FIG. 2: The measured differential jet shape, $\rho(r/R)$, in inclusive jet production for jets with $0.1 < |Y^{\text{jet}}| < 0.7$ and $37 \text{ GeV}/c < P_T^{\text{jet}} < 148 \text{ GeV}/c$, is shown in different P_T^{jet} regions. Error bars indicate the statistical and systematic uncertainties added in quadrature. The predictions of PYTHIA-Tune A (solid lines) and HERWIG (dashed lines) are shown for comparison.

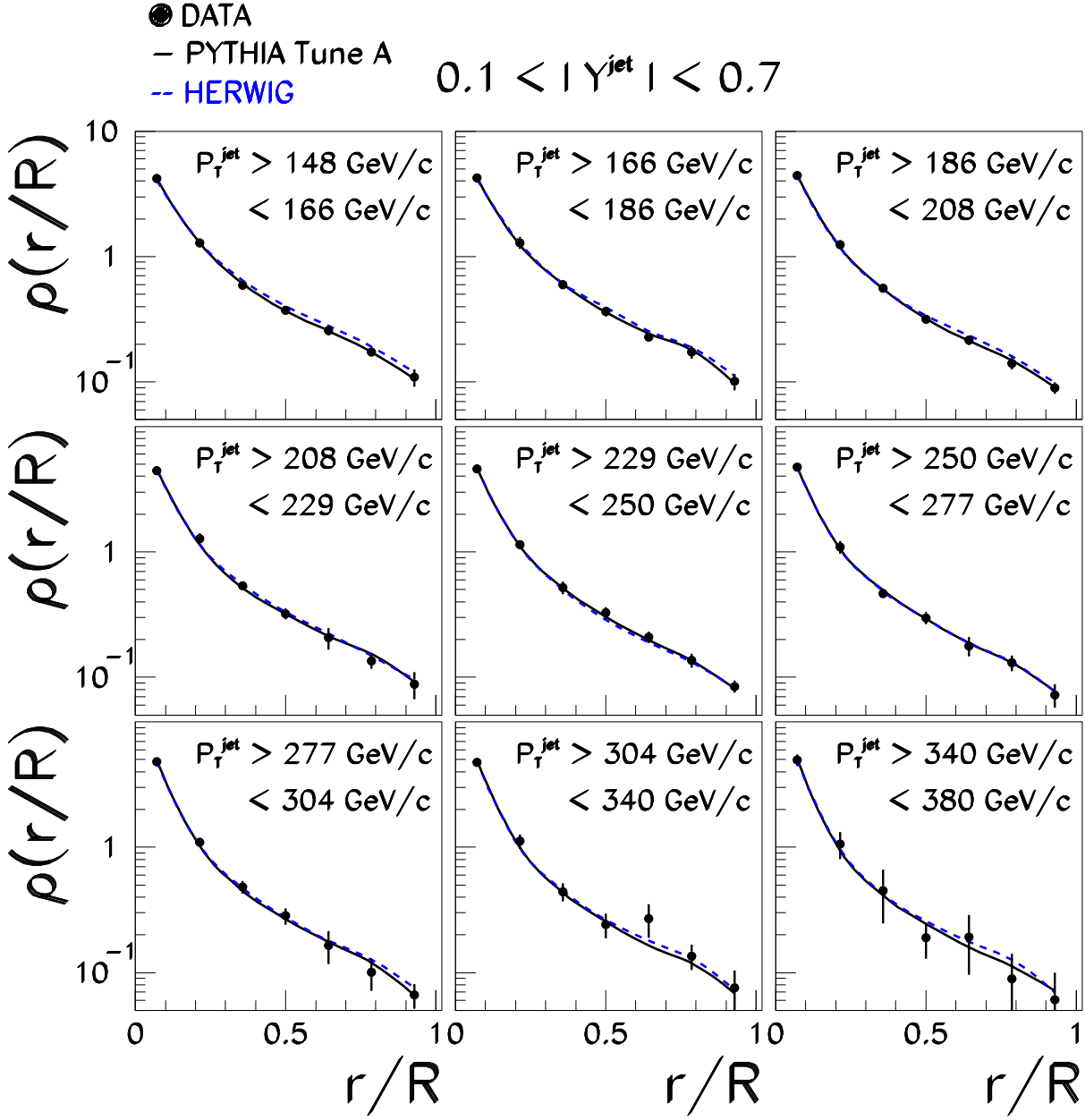


FIG. 3: The measured differential jet shape, $\rho(r/R)$, in inclusive jet production for jets with $0.1 < |Y^{\text{jet}}| < 0.7$ and $148 \text{ GeV}/c < P_T^{\text{jet}} < 380 \text{ GeV}/c$, is shown in different P_T^{jet} regions. Error bars indicate the statistical and systematic uncertainties added in quadrature. The predictions of PYTHIA-Tune A (solid lines) and HERWIG (dashed lines) are shown for comparison.

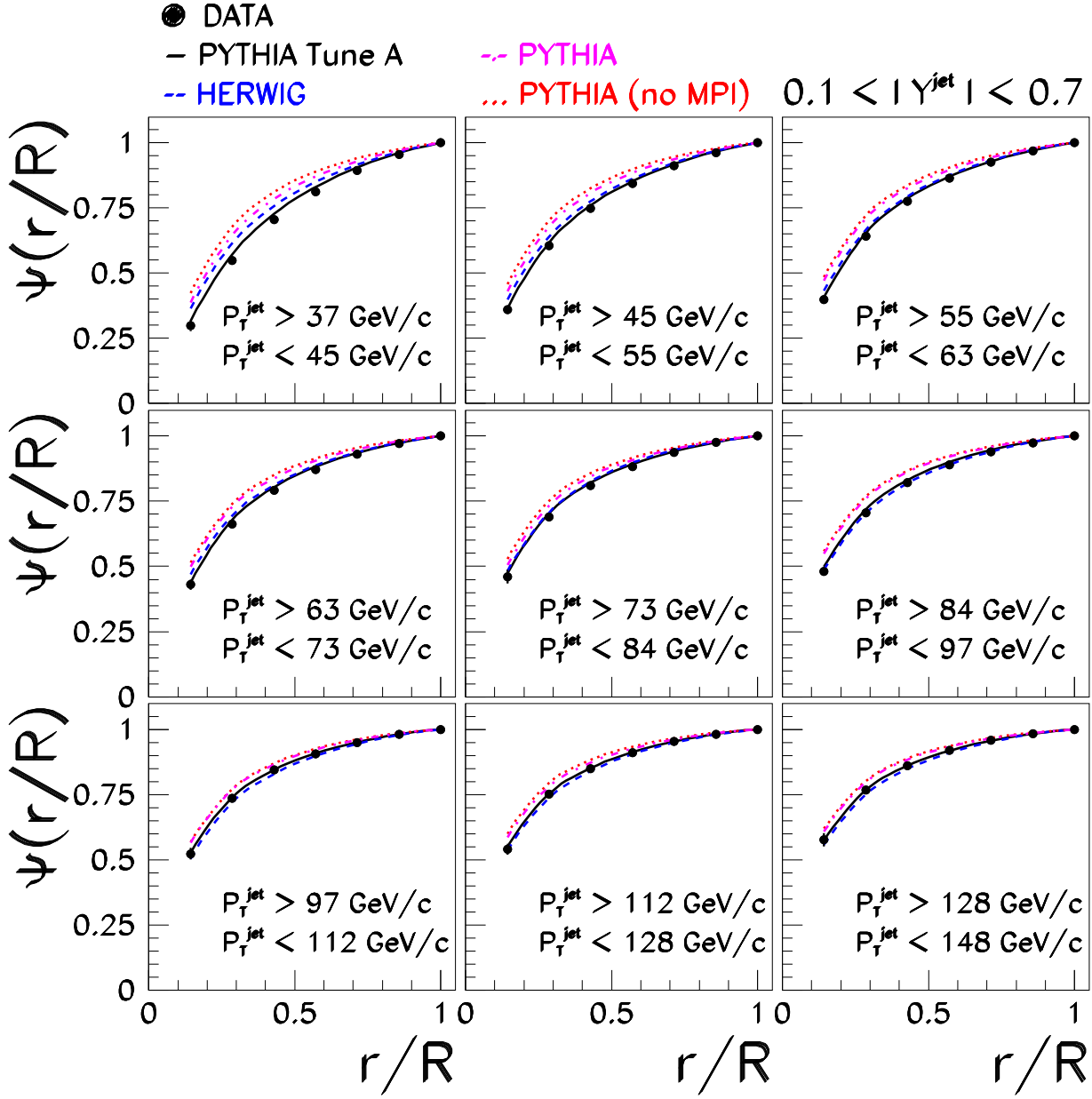


FIG. 4: The measured integrated jet shape, $\Psi(r/R)$, in inclusive jet production for jets with $0.1 < |Y^{\text{jet}}| < 0.7$ and $37 \text{ GeV}/c < P_T^{\text{jet}} < 148 \text{ GeV}/c$, is shown in different P_T^{jet} regions. Error bars indicate the statistical and systematic uncertainties added in quadrature. The predictions of PYTHIA-Tune A (solid lines), PYTHIA (dashed-dotted lines), PYTHIA-(no MPI) (dotted lines) and HERWIG (dashed lines) are shown for comparison.

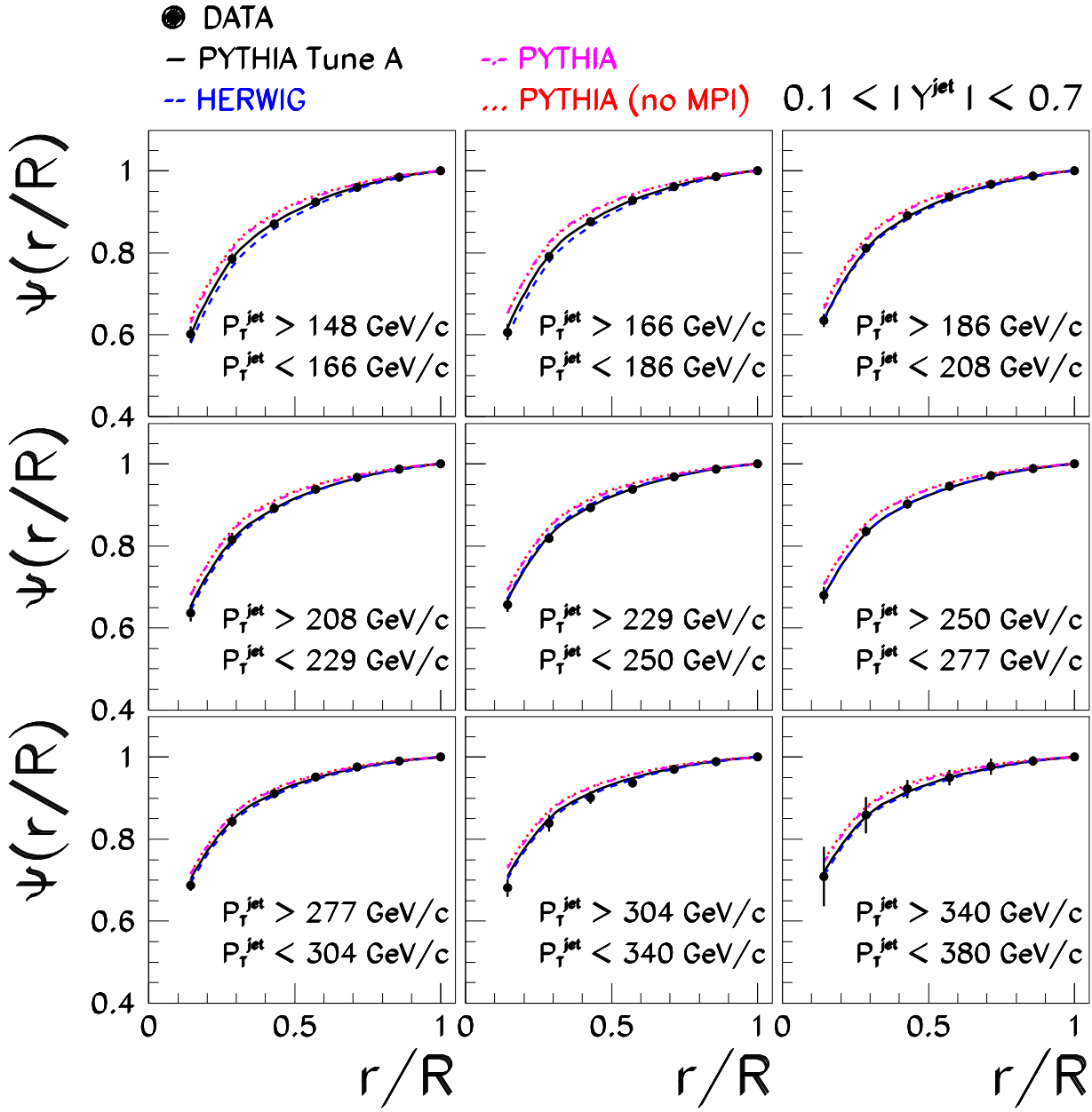


FIG. 5: The measured integrated jet shape, $\Psi(r/R)$, in inclusive jet production for jets with $0.1 < |Y^{\text{jet}}| < 0.7$ and $148 \text{ GeV}/c < P_T^{\text{jet}} < 380 \text{ GeV}/c$, is shown in different P_T^{jet} regions. Error bars indicate the statistical and systematic uncertainties added in quadrature. The predictions of PYTHIA-Tune A (solid lines), PYTHIA (dashed-dotted lines), PYTHIA-(no MPI) (dotted lines) and HERWIG (dashed lines) are shown for comparison.

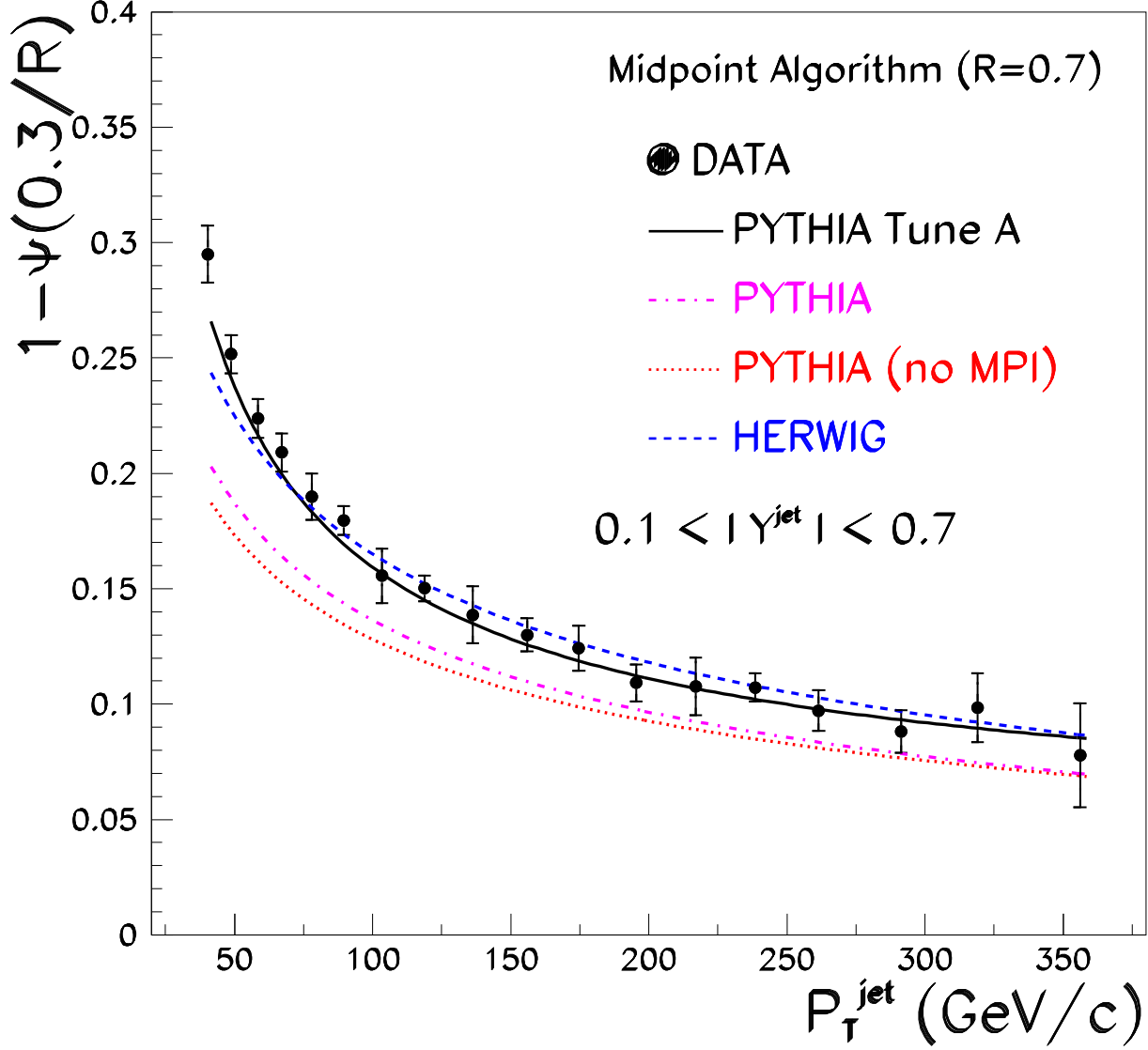


FIG. 6: The measured $1 - \Psi(0.3/R)$ as a function of P_T^{jet} for jets with $0.1 < |Y^{\text{jet}}| < 0.7$ and $37 \text{ GeV/c} < P_T^{\text{jet}} < 380 \text{ GeV/c}$. Error bars indicate the statistical and systematic uncertainties added in quadrature. The predictions of PYTHIA-Tune A (solid line), PYTHIA (dashed-dotted line), PYTHIA-(no MPI) (dotted line) and HERWIG (dashed line) are shown for comparison.

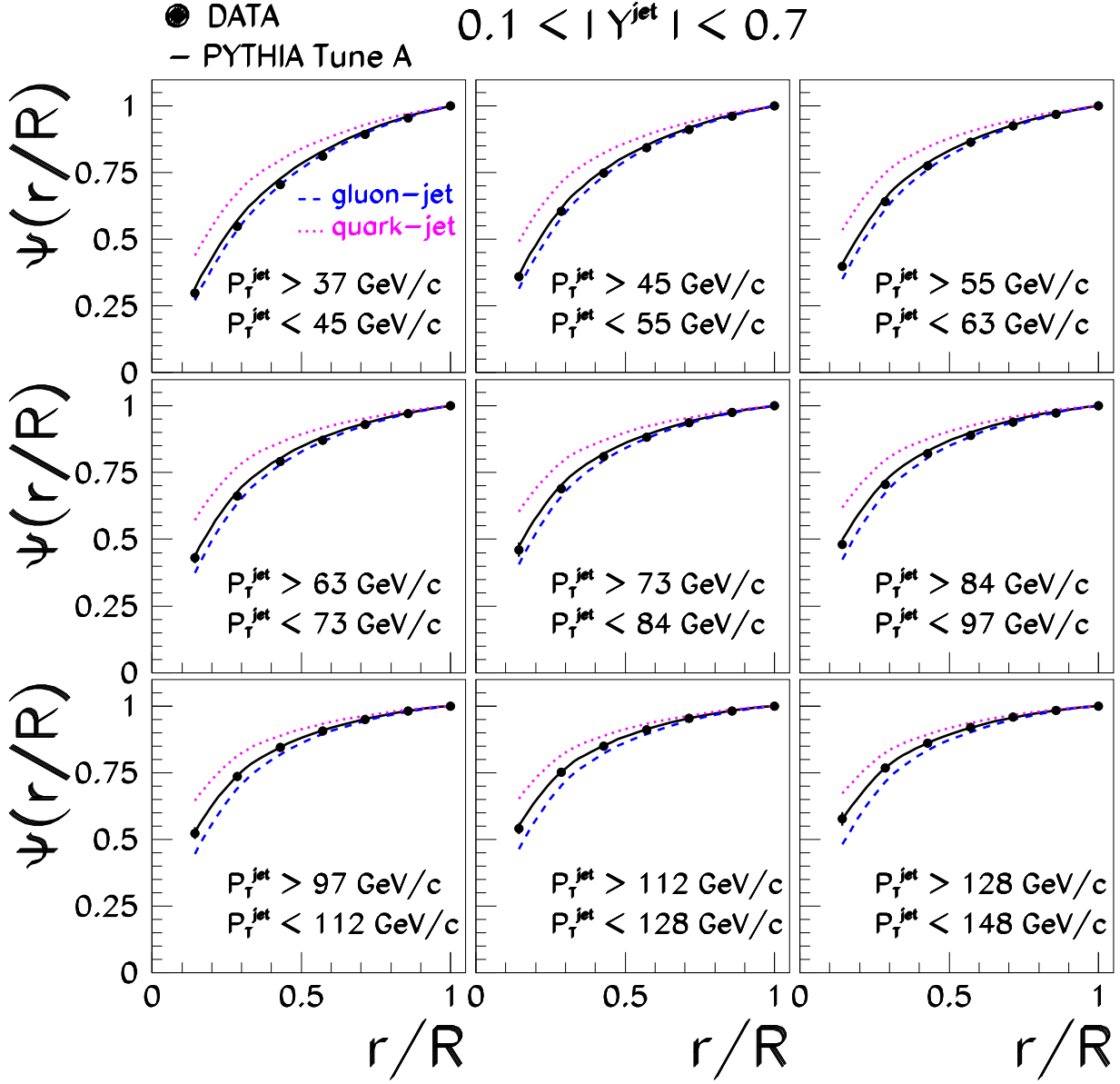


FIG. 7: The measured integrated jet shape, $\Psi(r/R)$, in inclusive jet production for jets with $0.1 < |Y^{\text{jet}}| < 0.7$ and $37 \text{ GeV/c} < P_T^{\text{jet}} < 148 \text{ GeV/c}$, is shown in different P_T^{jet} regions. Error bars indicate the statistical and systematic uncertainties added in quadrature. The predictions of PYTHIA-Tune A (solid lines) and the separate predictions for quark-initiated jets (dotted lines) and gluon-initiated jets (dashed lines) are shown for comparison.

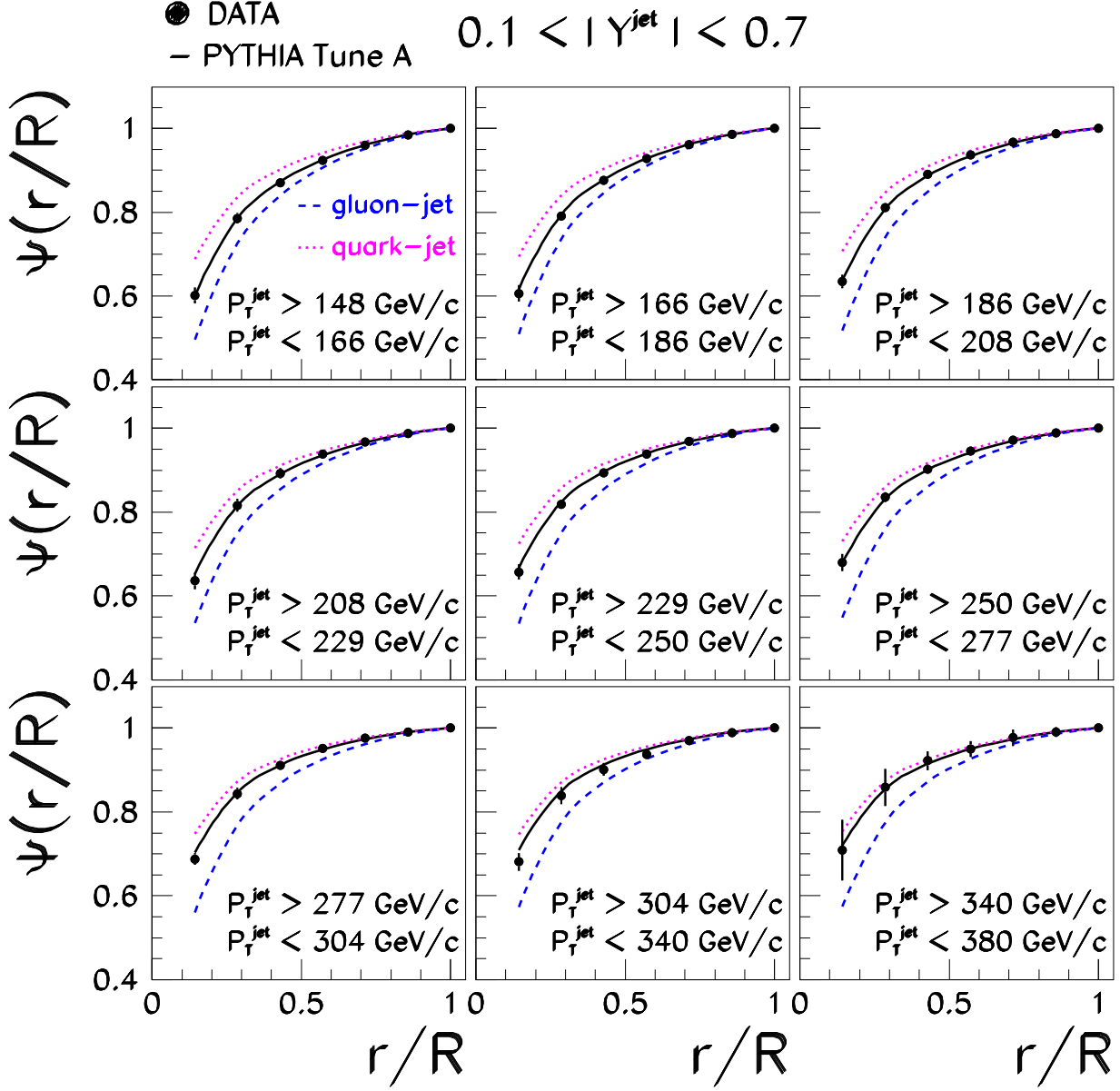


FIG. 8: The measured integrated jet shape, $\Psi(r/R)$, in inclusive jet production for jets with $0.1 < |Y^{\text{jet}}| < 0.7$ and $148 \text{ GeV}/c < P_T^{\text{jet}} < 380 \text{ GeV}/c$, is shown in different P_T^{jet} regions. Error bars indicate the statistical and systematic uncertainties added in quadrature. The predictions of PYTHIA-Tune A (solid lines) and the separate predictions for quark-initiated jets (dotted lines) and gluon-initiated jets (dashed lines) are shown for comparison.

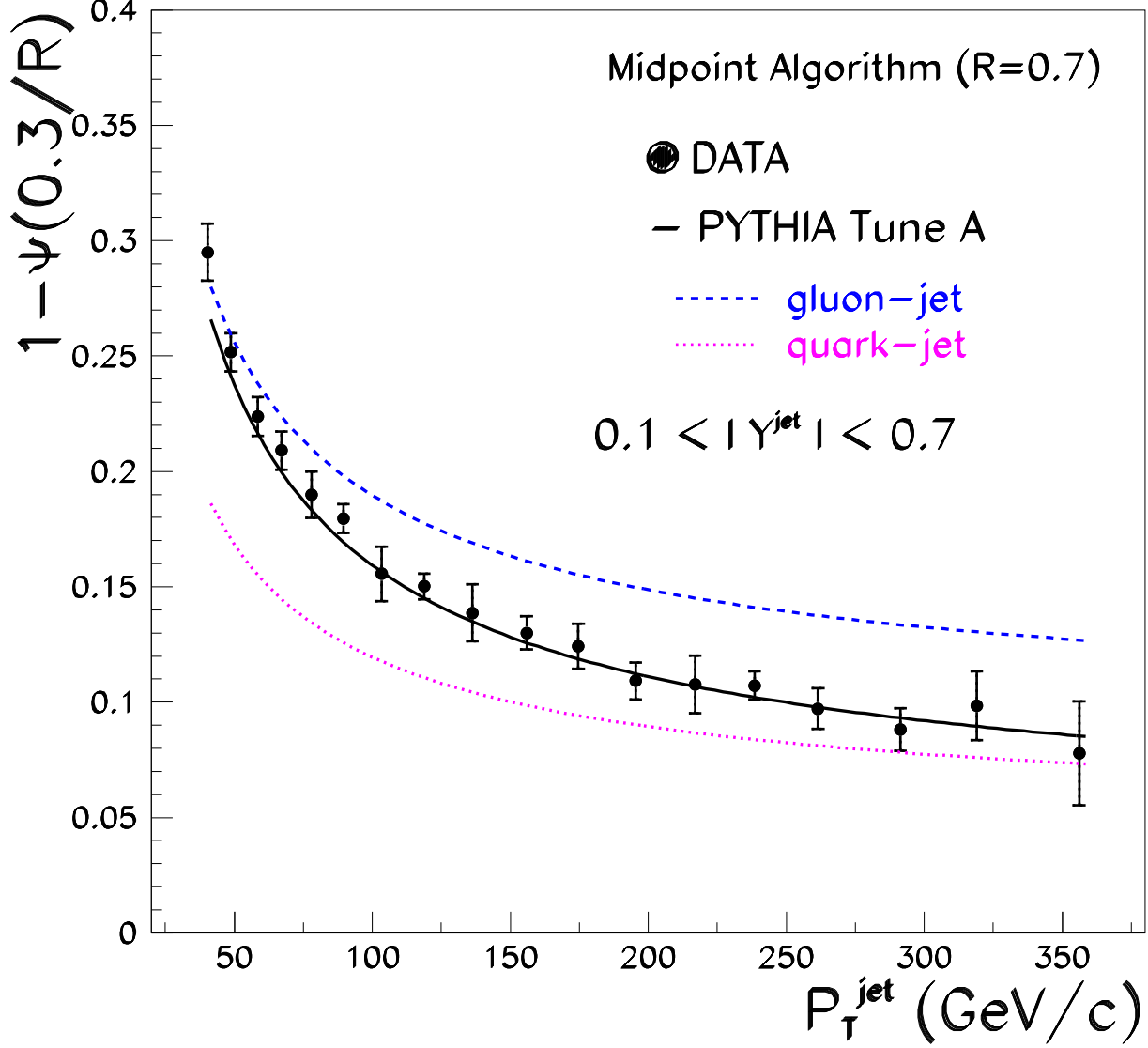


FIG. 9: The measured $1 - \Psi(0.3/R)$ as a function of P_T^{jet} for jets with $0.1 < |Y^{\text{jet}}| < 0.7$ and $37 \text{ GeV/c} < P_T^{\text{jet}} < 380 \text{ GeV/c}$. Error bars indicate the statistical and systematic uncertainties added in quadrature. The predictions of PYTHIA-Tune A (solid line) and the separate predictions for quark-initiated jets (dotted line) and gluon-initiated jets (dashed line) are shown for comparison.